

Parameters of the Magnetic Flux inside Coronal Holes

Valentyna Abramenko and Vasyl Yurchyshyn

Big Bear Solar Observatory, Big Bear City, CA 92314, USA

Hiroko Watanabe

Kwasan and Hida Observatories, Kyoto University, Kitakasan, Ohminecyou, Yamashina, Kyoto 607-8471, Japan

Abstract. Parameters of magnetic flux distribution inside low-latitude coronal holes (CHs) were analyzed. A statistical study of 44 CHs based on Solar and Heliospheric Observatory (SOHO)/MDI full disk magnetograms and SOHO/EIT 284Å images showed that the density of the net magnetic flux, B_{net} , does not correlate with the associated solar wind speeds, V_x . Both the area and net flux of CHs correlate with the solar wind speed and the corresponding spatial Pearson correlation coefficients are 0.75 and 0.71, respectively. A possible explanation for the low correlation between B_{net} and V_x is proposed. The observed non-correlation might be rooted in the structural complexity of the magnetic field. As a measure of complexity of the magnetic field, the filling factor, $f(r)$, was calculated as a function of spatial scales. In CHs, $f(r)$ was found to be nearly constant at scales above 2 Mm, which indicates a monofractal structural organization and smooth temporal evolution. The magnitude of the filling factor is 0.04 from the Hinode SOT/SP data and 0.07 from the MDI/HR data. The Hinode data show that at scales smaller than 2 Mm, the filling factor decreases rapidly, which means a multifractal structure and highly intermittent, burst-like energy release regime. The absence of necessary complexity in CH magnetic fields at scales above 2 Mm seems to be the most plausible reason why the net magnetic flux density does not seem to be related to the solar wind speed: the energy release dynamics, needed for solar wind acceleration, appears to occur at small scales below 1 Mm.

Keywords: Sun: magnetic fields, coronal holes, solar wind

1. Introduction

Since the Skylab mission in early 1970s, it is believed that the coronal holes seen on the surface of the Sun are related to the high-speed streams of the solar wind and they might be a cause of geomagnetic disturbances (see, *e.g.*, Sheeley *et al.* (1976) and references therein). A possibility of ground-based observations of coronal holes in the spectral line He 1083.0 nm (Harvey *et al.*, 1975) stimulated the interest to the problem. Numerous sophisticated models were proposed to explain the CHs formation and evolution (*e.g.*, Wang and Sheeley, 1991; Fisk, 1996, 2001, 2005; Fisk *et al.*, 1999; Wang *et al.*, 2000; Schrijver, 2001; Schrijver and Title, 2001; Schrijver *et al.*, 2002; Schrijver and DeRosa, 2003).



© 2021 Kluwer Academic Publishers. Printed in the Netherlands.

During the last decade, a connection between the coronal holes and various heliospheric phenomena, such as, high speed streams, corotating interaction regions, long-living geomagnetic storms without CMEs (see, *e.g.*, Vrsnak *et al.*, 2007 for references), became well established and stimulated elaboration of approaches to forecast the geomagnetic response to the transit of a coronal hole over the solar disk. An area occupied by coronal holes turned to be a very fruitful parameter. Robbins *et al.* (2006) suggested an empirical model to predict the solar wind speed at 1 AU from measurements of the fractional area occupied by a CH inside a 14° - sectorial region centered at the central meridian. A similar technique was independently applied later by Vrsnak *et al.* (2007) and further extended to forecast, along with the solar wind speed, other parameters of the solar wind, such as proton density, temperature and magnetic field strength at 1 AU.

Several groups analyzed properties of the magnetic fields inside coronal holes (*e.g.*, Harvey and Sheeley, 1979; Harvey *et al.*, 1982; Obridko and Shelting, 1989; Bumba *et al.*, 1995; Obridko *et al.*, 2000; Wiegmann and Solanki, 2004; Wiegmann *et al.*, 2005; Abramenko *et al.*, 2006; Hagenaar *et al.*, 2008). The most comprehensive study made so far on the net magnetic fluxes and averaged flux densities in coronal holes was presented by Harvey and colleagues (Harvey *et al.*, 1982), which was based on the Kitt Peak full disk magnetograms (1 arcsec pixel size) and hand-drawn maps of coronal holes derived from the He 1083.0 nm data. These authors analyzed the ascending phase of the 21st cycle and reported an increase in the averaged net flux density as the solar activity intensified. This was explained by an extra flux deposited into low-latitude coronal holes by decaying active regions. Since then, the density of the net flux inside CHs was adopted as a representative characteristic of the magnetic field inside coronal holes.

As long as it is the magnetic field that is ultimately responsible for energetics in a coronal hole, it would be interesting to explore how the density of the net magnetic flux is related to the speed of the fast solar wind. We performed such a statistical study on the basis of the MDI full disk magnetograms (Section 2) and found a rather surprising result: the density of the net flux is not correlated with the solar wind speed measured at 1 AU. What could be a reason for that? We suggested that the reason might be that the density of the magnetic flux, derived from low-resolution data and averaged over the CH's area, is not a suitable parameter to qualify energetics in CHs. The ultimate reason for the observed non-correlation might stem from the structural organization of the magnetic flux and its multifractal nature at small scales. This encouraged us to study multifractal properties of the magnetic flux inside a coronal hole taking advantage of the high

resolution Hinode observations of the magnetic field (Section 3). Our final section represents summary and discussion of the results.

2. Averaged Net Flux Density Versus the Solar Wind Speed

2.1. EVENT SELECTION

Here we focus on the distribution of the magnetic flux density of 44 CHs observed between March 2001 and July 2006 at low solar latitudes near the center of the solar disk (Table I). To avoid influence of the projection effect, we required that the angular distance, θ , from the disk center to the center of gravity of a CH should not exceed 20 degrees. The values of θ (positive when the gravity center was located in the northern hemisphere) are shown in the 8-th column of Table I. In the process of event selection we discarded all CHs that had more than 5% of their area outside a circle of 30 degree radius centered at the solar disk center.

We also made sure that the solar wind speed profiles were not contaminated by a possible influence of ICMEs. Following Arge *et al.* (2004), we selected only the events when, at the arrival time of the streams, the value of the plasma beta (<http://omniweb.gsfc.nasa.gov/form/dx1.html>) was well above 0.1.

For the selected 44 CHs (Table I), we utilized the following data sets: i) Michelson Doppler Imager (SOHO/MDI; Scherrer *et al.*, 1995) 1 min averaged full disk magnetograms (spatial resolution 4 arcsec and the pixel size of 2 arcsec); ii) Fe xv 284 Å images from the EUV Imaging Telescope (SOHO/EIT; Delaboudiniere *et al.*, 1995), and iii) ACE/SWEPAM and MAG measurements of the solar wind at 1 AU.

Each CH was determined in an EIT Fe xv 284 Å image as an area with pixel intensity below a certain threshold, namely, 80 DN. The threshold level was first determined by trial-and-error method for one CH and it remained the same for all the CHs analyzed here. Next, we co-aligned the EIT image, taken at the time when the CH passed the central meridian with the closest MDI magnetogram. The CH boundary was then mapped on that magnetogram, and calculations of the magnetic field statistics were performed for an ensemble of pixels enclosed by this boundary (Figure 1). In cases when the time difference between the EIT image and the corresponding magnetogram exceeded 1/2 hour, we aligned the images taking into account the differential rotation of the Sun. We discarded all events where the time difference between the EIT and MDI images exceeded 4 hours.

One more criteria was used to ensure that a given CH is indeed associated with the feature observed in the solar wind speed profile. In case of the positive association, the polarity of the B_x component of the solar wind magnetic field, measured in the GSE coordinate system by ACE/MAG, should be opposite to that of the open flux in the base of the CH because the x -axis in the GSE system points from the Earth toward the Sun, while the positive magnetic field on the solar surface is directed outward from the Sun. Only those CHs, for which magnetic polarities satisfied the above condition, were included into this study.

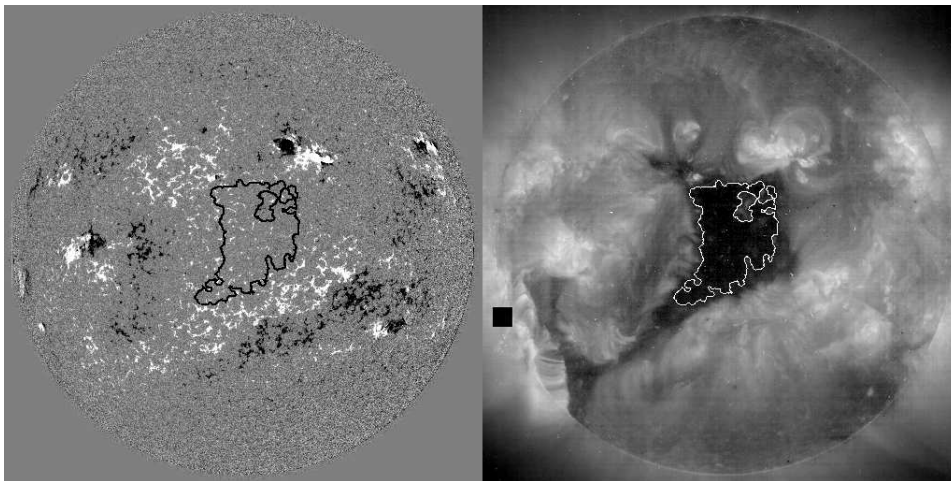


Figure 1. SOHO/MDI magnetogram (left) and the corresponding SOHO/EIT 284 Å image taken at 19:06 UT on 2 March 2002 (right). The contour indicates the boundary of coronal hole CH201 (see Table I).

2.2. SOLAR WIND SPEED DERIVATION

For each CH in our data set, we determined the solar wind speed, V_x . We utilized the 64 s averaged time profiles measured in the GSE coordinate system with ACE/SWEPAM instruments. Note that the solar wind speed acquires negative values in the GSE coordinate system.

The arrival time at 1 AU of the solar wind associated with the CH was determined as the moment t , when a function

$$\Delta r(t) = V_x(t - t_0) - 1\text{AU} \quad (1)$$

turns into zero. Here, t_0 (3rd column of Table I) is the CH culmination time, and $t = t_A$ (4-th column of Table I) is the arrival time.

We then accepted that the association between the CH and the solar wind feature is reliable when t_A , calculated from Equation (1), falls into the well pronounced “dip” in the observed solar wind speed

profile. Figure 2 shows an observed time profile of the solar wind speed and the corresponding profile of $\Delta r(t)$ associated with the CH shown in Figure 1.

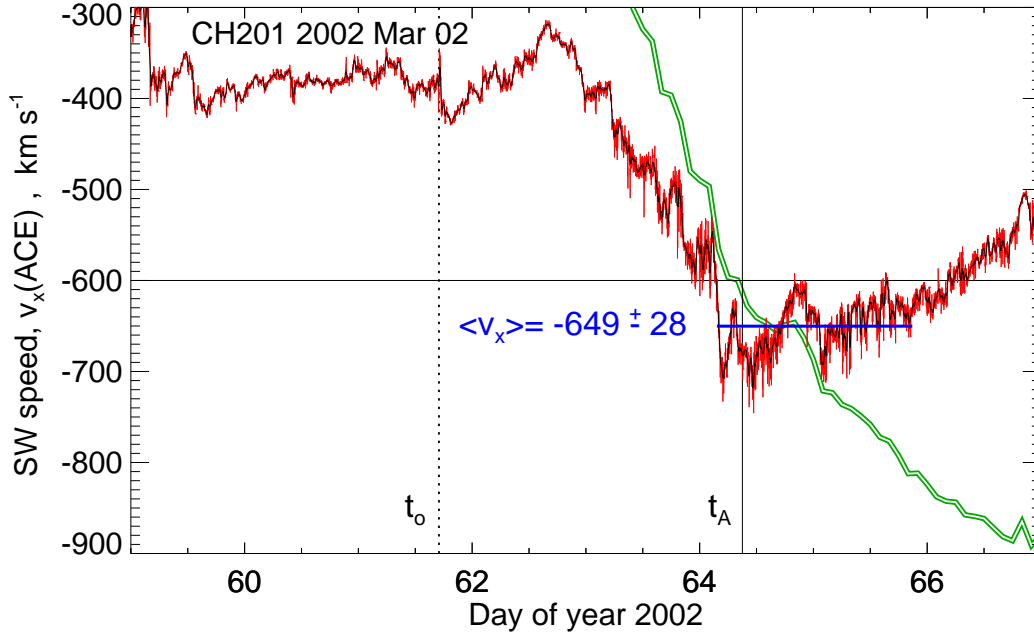


Figure 2. Observed time profile of the V_x component of the solar wind speed (red curve) as measured by ACE satellite from 0000UT on 28 February 2002 until 2359UT on 7 March 2002. The black curve represents a smoothed over 21-point observed speed profile. The vertical dotted line indicates the CH culmination time, t_0 , while the vertical solid line indicates the solar wind arrival time, t_A . The arrival time was determined as the moment when parameter Δr (double green curve) is equal to zero. The blue thick horizontal line segment shows the time interval used to determine the average, for a given event, solar wind speed, $\langle V_x \rangle$ (indicated by the vertical position of the blue line segment).

The magnitude of the solar wind speed, $\langle V_x \rangle$, was determined by averaging the observed time profile of $V_x(t)$ over a time interval that includes the minimum of the observed speed profile. This time interval (marked by the thick blue horizontal segment in Figure 2) was defined in the following way. First, we applied a 21-point running averaging to the observed $V_x(t)$ profile (red curve in Figure 2). This smoothed profile (black curve) was then used to determine i) the level of undisturbed slow-wind speed, V_0 , preceding the CH, and ii) the maximum speed inside the CH, V_{\max} . To obtain the averaged solar wind speed, $\langle V_x \rangle$,

we averaged all data points inside an interval where $V_x(t)$ is lower than $V_{\max} + (|V_{\max}| - |V_0|)/4$. This threshold was chosen by a trial-and-error method. The resulting averaged solar wind speed is indicated in Figure 2 by the vertical position of the blue line segment. We would like to emphasize here that we did not include in our study those CHs whose associated speed profile was so complex that no well defined minimum could be chosen.

For each CH in our data set, the area of the CH (in pixels of the MDI full disk magnetogram) and the associated solar wind speed are listed in the 7-th and 9-th columns of Table I, respectively.

The above routine allowed us to determine the arrival time and the magnitude of the solar wind speed individually for each coronal hole. This technique differs from that applied by Robbins *et al.* (2006) and Vrsnak *et al.* (2007), where the mean arrival time, determined from the cross-correlation technique, was utilized.

2.3. MAGNETIC PARAMETERS

The above selection routine left us with a set of 44 CHs. MDI full disk 1 minute average magnetograms were available for all of them. However, the full disk data of 1 minute cadence, as well as the observations in the MDI high resolution mode, were not available for all of them. Since we are interested in measurements of the net magnetic flux density, we decided first to focus on whether the measurements of this parameter from 1 minute full disk magnetograms are reliable. To do that, we analyzed coronal hole CH 204 from our data list (see Table I), for which nearly simultaneous observations in two MDI modes were available: 1 minute cadence full disk and high resolution modes. Inside this large coronal hole, located at the solar disk center, we outlined a rectangular area of $n \times m$ pixels and calculated magnetic parameters for five different magnetograms. Results are compiled in Table II, where the first row is the result from one original individual MDI full disk 1 minute magnetogram. The second row represents results from the same magnetogram, but smoothed in both directions with a boxcar average of three pixels. The third row are parameters from a magnetogram derived from averaging of five consecutive original 1 min magnetograms, whereas its smoothed version is presented in the next row. The last row represents results from the high resolution MDI magnetogram recorded at the same place on the Sun with pixel size of 0.6 arcsec.

From each of the above magnetograms, we first calculated the net flux density, $B_{\text{net}} = \sum B_{\parallel} / (n \times m)$ (2nd column in Table II), inside the box. We note that the net flux is obtained by summing all pixel values with their sign. This procedure results in cancellation of the bulk of

sign-variable noise. Magnetic flux confined in loops, closed within the CH, will also be canceled. This allowed us to assume that in CHs, the net flux density also represents the open magnetic flux density.

The density of the total unsigned flux, $B_{\text{tot}} = \sum |B_{\parallel}| / (n \times m)$, is shown in the 3rd column of Table II. The 4-th column represents the density, B_{n} , of the noise in magnetograms derived from the power spectrum calculations as it was suggested by Longcope and Parnell (2008). To derive this parameter, we calculated a 1D power spectrum, $S(k)$, from each magnetogram and then calculated the noise density as $B_{\text{n}} = (\pi k_c^2 S(k_c))^{1/2}$, where $k_c = 2\pi^{1/2} \Delta x$ is the maximum wave number. The imbalance of the magnetic flux is shown in the 5-th column. The 6-th column represents the density of the net flux calculated over the area where $|B_{\parallel}| < 3B_{\text{n}}$ (we denote $3B_{\text{n}} = p$), and the last column shows the fraction of the box area, where the flux density exceeds the triple noise level, $|B_{\parallel}| > p$.

Data of Table II indicate that the density of the net flux, B_{net} , does not vary much (by less than 2%) with temporal/spatial averaging and does not depend on the noise level. At the same time, the density of the unsigned flux, B_{tot} , depends significantly on the noise level. (Note that the magnitude of B_{n} is in good agreement with the results from MDI full disk data noise reduction reported by Hagenaar *et al.* (2008)). Last two columns in Table II show that the bulk of the magnetic flux in CHs is concentrated within a small (a few percents) fraction of the CH's area. Vast zones of low fluctuations contribute only about 1 G into the resulting magnitude (4 G) of the net flux density.

This experiment shows, first, that an averaging procedure is undesirable when one intends to analyze fine structures of the magnetic field. Second, that the net flux density in coronal holes is measured with the same level of confidence from the original and averaged magnetograms. High noise level in original magnetograms does not influence much on the B_{net} calculations. The reasons for that are: i) high imbalance of the magnetic flux inside coronal holes, accompanied by low (as compared to adjacent quiet sun areas) rate of dipole emergence (Abramenko *et al.*, 2006; Hagenaar *et al.*, 2008); and ii) magnetic features that contribute to the open flux are predominantly well above the noise level, even for the noisiest magnetogram.

For 44 coronal holes analyzed here, magnitudes of the net magnetic flux, $\Phi_{\text{net}} = \sum B_{\parallel} \Delta s$, where Δs is a pixel size, are presented in the 5-th column of Table I. The 6-th column shows the densities of the net magnetic flux, $B_{\text{net}} = \sum B_{\parallel} / A$, where A is the area in pixels inside the CH boundary, 7-th column in Table I. We would like to emphasize that the moduli of B_{net} tend to decrease from March 2001 toward July 2006,

i.e., toward the end of the 23rd cycle. This is in qualitative agreement with Harvey *et al.* (1982).

2.4. CORRELATIONS BETWEEN CALCULATED PARAMETERS

Figure 3 shows correlations between parameters of CHs and the solar wind speed. The solar wind speed, $\langle V_x \rangle$, is directly correlated with the total net flux (upper left panel). The corresponding Pearson coefficient is 0.71 and the linear fit is given by

$$\langle V_x \rangle = 494 + 47.4 \cdot \Phi_{\text{net}}, \quad (2)$$

where $\langle V_x \rangle$ is in km s^{-1} and Φ_{net} is in 10^{21} Mx.

However, the total net flux is a product of the CH area, A , and the average net flux density, B_{net} . According to Figure 3, the solar wind speed is strongly correlated with the CH area (upper right panel, correlation coefficient (cc)=0.75) and only weakly depends on the averaged net flux density (lower left panel, cc=0.20). Linear fitting to the data point gave us the following relationship between the speeds and CH areas:

$$\langle V_x \rangle = 486 + 8.50 \cdot A, \quad (3)$$

where A is in 10^4 arcsec². As a result, there is a very strong dependence of the total net magnetic flux from the CH area (cc=0.92, lower right panel), which allows a reliable estimation of the total open flux in a CH:

$$\Phi_{\text{net}} = 0.045 + 0.156 \cdot A, \quad (4)$$

where Φ_{net} is in 10^{21} Mx and A is in 10^4 arcsec².

These findings very well agree with previously reported results (Wang and Sheeley, 1990; Robbins *et al.*, 2006; Vrsnak *et al.*, 2007; Schwadron and McComas, 2008) in spite of differences in used techniques. This consistency indicates reliability of the coronal hole analysis presented here.

On many occasions, analyzed CHs had closed loop structures embedded within them, which, in general, reduces the area occupied by the open flux and may lead to different magnitudes of the averaged total flux density. We excluded the closed loop areas from our calculations and repeated the above analysis. As expected, since the closed loop regions substitute a small fraction of the CH area, accounting for them did not lead to a significant change of the relationship between the solar wind speed and the total flux density. In fact, the Pearson coefficient even slightly decreased to 0.15.

We finally would like to note that the well defined relationship between the speed and area opens up a possibility to estimate the solar

wind speed 3-4 days in advance by measuring the area of a CH, when it passes the central meridian. (Note that in this study the CH area was measured inside a contour of 80 DN in EIT/Fe xv 284 Å images.)

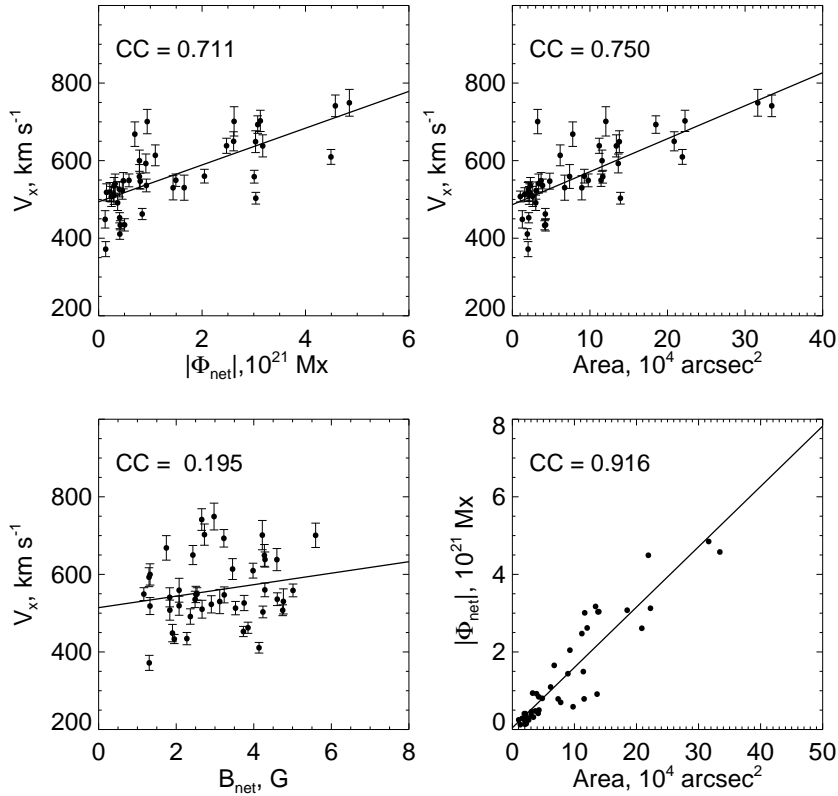


Figure 3. Correlations between magnetic parameters of coronal holes and solar wind parameters. Solid straight lines represent the best linear fit to the data points.

3. Multifractality in the Magnetic Field in Coronal Holes

The absence of a relationship between the solar wind speed and the density of the magnetic flux, seems to be suspicious at the first sight. The solar wind speed represents the intensity of the solar wind acceleration processes, *i.e.*, energy release dynamics, which ultimately is related to the magnetic field. Numerous recent studies of the dynamics of energy release in the low corona based on Hinode data (Baker *et al.*, 2008; Suematsu, 2008; Shimojo, 2008; Moreno-Insertis *et al.*, 2008) tell

us that there is a role for the magnetic field to play in these phenomena. Two things could be done to resolve the problem. First, improve spatial resolution of magnetic field measurements, and second, explore the proper measures of complexity of the magnetic field.

The Solar Optical Telescope (SOT, Tsuneta *et al.*, 2008) onboard *Hinode* has a 50 cm aperture mirror and is the largest optical solar telescope ever sent to space. The Hinode/Spectropolarimeter (SP, Ichimoto *et al.*, 2008) obtains the full Stokes parameters using the Fe I 630 nm absorption line and offers a unique opportunity to obtain magnetograms with pixel size of 0.32 arcsec in the fast mode and 0.16 arcsec in the normal mode. Coronal holes at low latitudes are rare during a solar minimum, where we are now. Nevertheless, on 11 November 2008 the SOT/SP instrument recorded a CH (Figure 4) at the disk center in the fast mode. We analyzed here one of the SOT/SP magnetograms of 942×500 pixels taken in the fast mode (Figure 5). The inversion code and calibration routine were performed at HAO CSAC ([http : //www.csac.hao.ucar.edu/](http://www.csac.hao.ucar.edu/)). The magnetogram was carefully despiked.

It is believed now that magnetic structures in active regions and in quiet sun areas are fractals (Tarbell *et al.*, 1990; Schrijver *et al.*, 1992; Balke *et al.*, 1993; Lawrence *et al.*, 1993; Meunier, 1999; Ireland *et al.*, 2004; Janssen *et al.*, 2003; McAteer *et al.*, 2005). In particular, Meunier (1999) and McAteer *et al.* (2005) showed that magnetic structures of active regions, even those recorded with 4 arcsec resolution (MDI full disk magnetograms), are fractals. Janssen *et al.* (2003) showed that the magnetic field in a quiet sun area is also a fractal. Fractals are self-similar, porous structures with jagged boundaries. Their scaling parameters do not vary with spatial scale. For example, the filling factor, *i.e.*, the ratio of the area occupied by (above-noise) fields to the entire area, does not vary when the resolution changes. An example: a comparison of the 3rd and 5-th rows in the last column in Table II tell us that the fraction of the area occupied by strong fields is nearly the same, about 6%, for the 4 arcsec and 1.2 arcsec resolutions. This might indicate that the coronal hole magnetic field structure at these scales can be considered as a single fractal, or, in other words, a *monofractal*.

Temporal variations in monofractal structures are non-intermittent, *i.e.*, high fluctuations in energy release are very rare and they do not represent a burst-like behavior. Therefore, strong energy release events are rare and they do not define the energy balance dynamics.

Another situation is when a multifractal is formed. Multifractals form in nature ubiquitously when several processes contemporaneously govern formation of a structure, each one dictating its own rules of clustering and fragmentation. A highly intermittent temporal behavior

is inherent for multifractals, so that high fluctuations in energy release are not rare, and the regime of violent, burst-like energy release dynamics is set. Therefore, to relate the energy release dynamics with the magnetic field, one should find the spatial scales where multifractal properties of the magnetic field manifest themselves, if any. (Note that the terms multifractality and intermittency describe the same property of a structure. However, the former is related to the spatial domain while the later is usually utilized for the temporal domain; see, *e.g.*, Abramenko (2008) for details.)

One of possible ways to diagnose multifractality is based on calculation of the filling factor as a function of spatial scale (Frisch, 1995). For multifractals, the filling factor decreases as the scale decreases. In other words, the fraction of a volume occupied by strong fields (the so called active mode), decreases as we study the multifractal at smaller and smaller scales. For monofractals, this ratio is constant with scale. To this end, our goal was to explore how the filling factor varies with scale inside coronal holes.

The ratio of the active mode to the entire volume as a function of the scale, r , can be calculated from the flatness function, which for the longitudinal magnetic field B_l , can be written as (Frisch, 1995):

$$F(r) = S_4(r)/(S_2(r))^2. \quad (5)$$

Here,

$$S_q(r) = \langle |B_l(\mathbf{x} + \mathbf{r}) - B_l(\mathbf{x})|^q \rangle \quad (6)$$

are the structure functions, and \mathbf{x} is the current pixel on a magnetogram, \mathbf{r} is the separation vector (*i.e.*, the spatial scale), and q is the order of a statistical moment, which takes on real values. The angular brackets denote averaging over the magnetogram. Details of the calculation routines and applications can be found in Abramenko *et al.* (2002, 2003, 2008) and in Abramenko (2005). The filling factor is then calculated as

$$f(r) = 1/F(r). \quad (7)$$

As it was mentioned above, the filling factor does not depend on the spatial scale, r , in case of a monofractal structure. On the contrary, for a multifractal, the filling factor displays a power-law decrease as the scales become progressively smaller.

Results of the filling factor are presented in Figure 6. Hinode/SOT/SP data for the CH observed on 30 November 2008 (blue curve) indicates that at scales larger than approximately 2 Mm, the magnetic field structure seems to be a monofractal. Only a very slight slope (0.024) of the power law linear fit is observed. Thus, at scales larger than 2 Mm, the magnetic field in a coronal hole seems to be a monofractal.

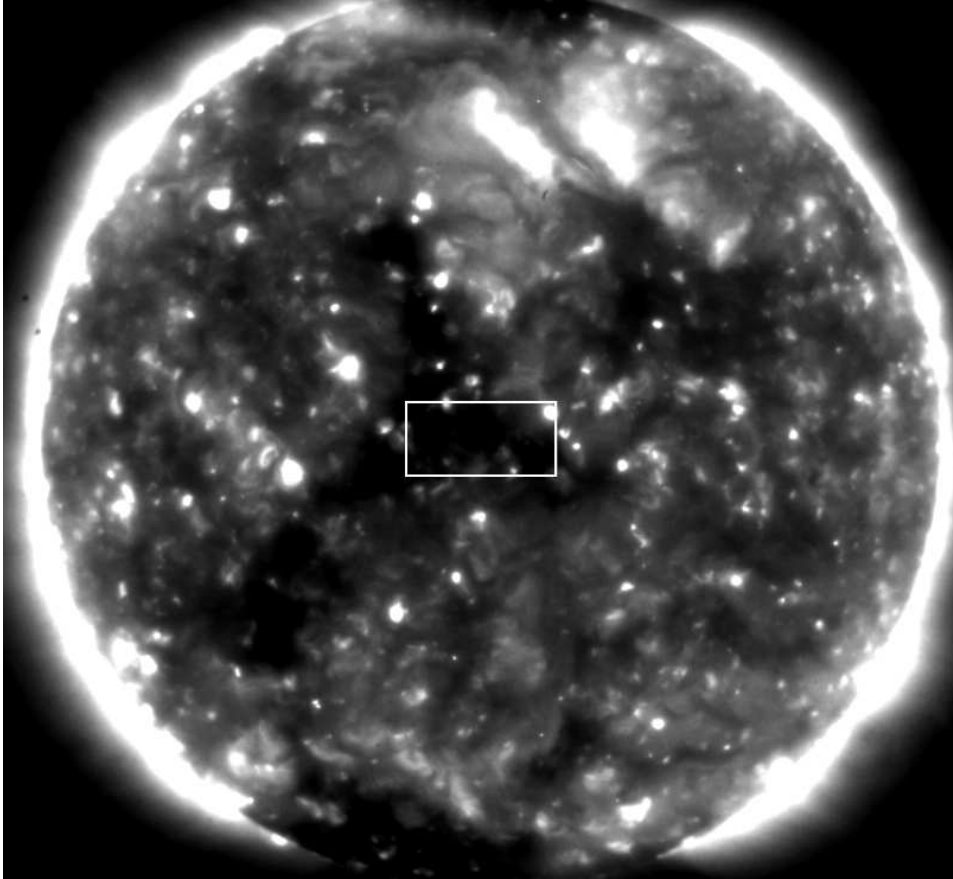


Figure 4. The 11:42UT XRT image on 30 November 2008. The box in the center of the solar disk outlines the area inside a coronal hole where the SOT/SP magnetogram was taken (Figure 5).

For comparison, we calculated and plotted in the same graph (Figure 6) the filling factor for an active region NOAA 0930 and a plage area to the west of this active region. The corresponding magnetograms were also derived with the SOT/SP instrument in the fast mode and processed with the same routines as those applied for the CH magnetogram. Data for the AR and plage show a steeper slope of the power law linear fit with indices of 0.18 and 0.09, respectively. The dependence of the filling factor on the scale implies multifractality of the magnetic field at scales larger than 2 Mm.

To double check our inference on monofractality in CHs at large scales, we calculated the filling factor from the MDI/HR data for 36 square areas located inside 19 coronal holes observed during 2002-2004 at the solar disk center. The MDI results are shown in Figure 6 with the

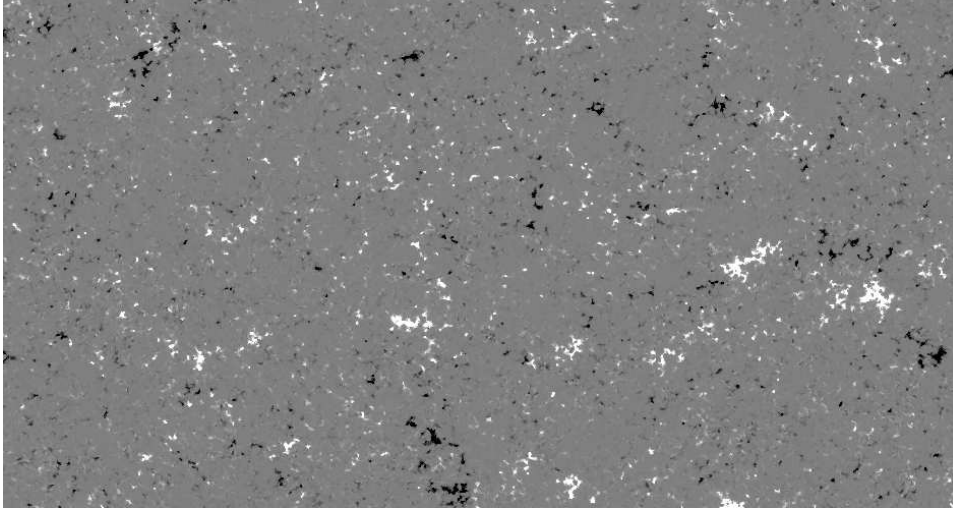


Figure 5. Hinode SOT/SP magnetogram of the coronal hole area outlined in Figure 4 obtained in the fast mode (pixel size of 0.297×0.320 arcsec) and calibrated with the HAO inversion code. The magnetogram was despiked. The size of the solar surface is 200×115 Mm. The image is scaled in the range from -500 to 500 G.

dotted line. At scales larger than approximately 3 Mm, the filling factor is constant, which confirms our inference on the monofractality of the coronal hole magnetic field. At spatial scales smaller than $r \approx 3$ Mm the filling factor function is influenced by noise and resolution of the MDI data and it tends to grow as the scale decreases. This effect is caused by the Gaussian nature of the data noise, with its intrinsic filling factor of $1/3$.

What is interesting is that the Hinode data do not show similar behavior of the filling factor at the same scales, $r < 3$ Mm. Instead, below $r = 2$ Mm, the Hinode SOT/SP filling factor displays a rapid decrease, which does not seem to be caused by data noise. The decrease of $f(r)$ is well pronounced for the coronal hole, an active region and plage area data.

The break in the filling factor function is observed at scales approximately of 1 Mm. We may conclude that below this scale, the CH magnetic field is a multifractal.

4. Summary and Discussion

In summary, analyzing magnetic fields inside the low-latitude coronal holes, we arrived at the following conclusions.

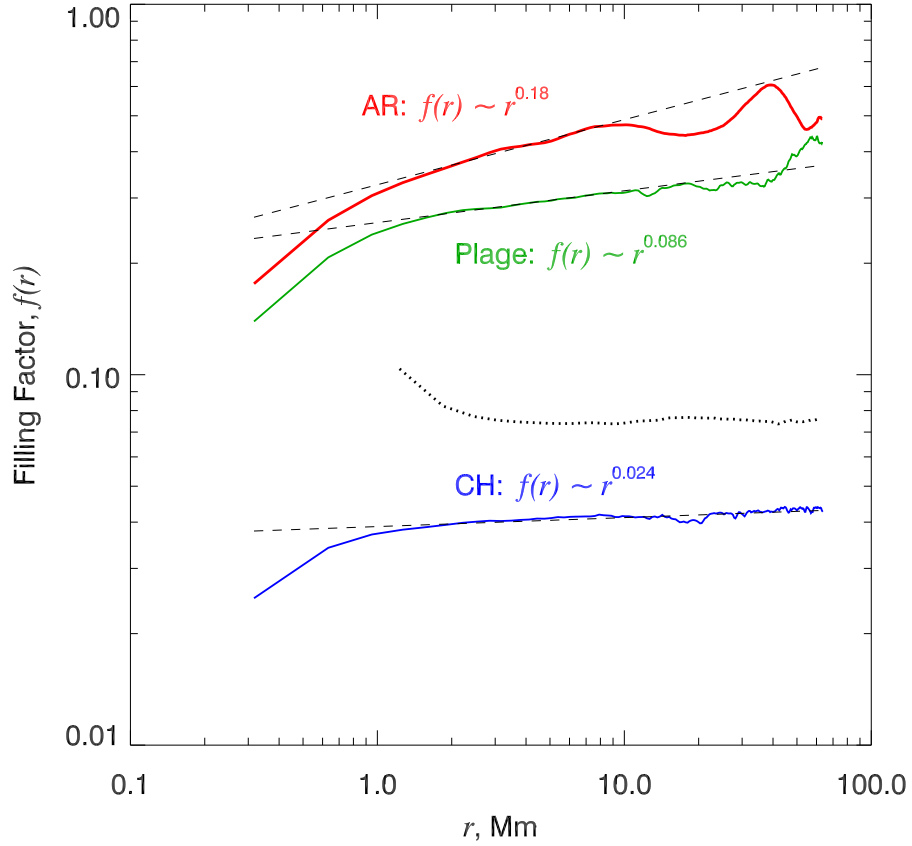


Figure 6. Variation of the filling factor, f , with spatial scale, r . Blue - data from the Hinode/SOT/SP magnetogram of the coronal hole shown in Figure 5. Black dots - the averaged filling factor calculated from 36 magnetograms for 19 coronal holes observed between 2002 and 2004 with SOHO/MDI in the high resolution mode. The flat filling factor is observed at scales above 3 Mm in both data sets. The decreasing of the filling factor at scales below 2 Mm is observed in SOT/SP data. For comparison, data for the active region NOAA 0930 (red) and weak plage area (green) derived from the Hinode/SOT/SP fast mode magnetograms are shown. The active region and the plage area display the decreasing filling factor at large scales above 2 Mm. Dashed lines represent the best linear fit to the data points inside an interval of $\Delta r = (1.6 - 8.2)$ Mm. The steeper slope of the fit corresponds to higher degree of multifractality.

i) The density of the net magnetic flux does not correlate with the corresponding *in situ* solar wind speeds. At the same time, both CH area and total net flux correlate very well with the solar wind speed and the corresponding spatial Pearson correlation coefficients determined

for 44 CHs are 0.75 and 0.71, respectively. The relationship between the CH areas and the solar wind speed with almost the same results in correlation was earlier derived by Robbins *et al.* (2006) and by Vrsnak *et al.* (2007).

As we discussed in Section 1, the fact that the net magnetic flux density is not correlated with the solar wind speed can hardly be interpreted as irrelevance of the magnetic field to the solar wind acceleration process. One would rather suggest that the net flux density measured with the resolution of 4 arcsec does not reflect the energy release dynamics inside CHs. Analysis of SOHO/MDI/high-resolution and Hinode/SOT/SP magnetograms seems to support this suggestion.

ii) The filling factor as a measure of multifractality in CHs was calculated as a function of spatial scale. It was found to be nearly constant at scales above 2 Mm. Its magnitude is approximately 0.04 from the Hinode data and 0.07 from the MDI/HR data. At scales smaller than 2 Mm, the filling factor starts to decline as the scale becomes smaller, and at approximately 1 Mm the regime of fast decrease of the filling factor is set.

A constant filling factor at $r > 2$ Mm in the CH magnetic fields indicates their monofractal nature and self-similarity. A self-similar structure by definition possesses constant statistical parameters at all scales (such as various scaling exponents, including the filling factor). However, only for artificial, mathematically created fractals, self-similarity is present at infinite range of scales (see, *e.g.*, Schroeder, 1991). For a majority of structures in nature, however, self-similarity with constant scaling parameters only holds at a finite range of scales, while at the entire interval of scales the scaling parameters are different. As a result, a multifractal structure forms with a superposition of many fractals, each one imposing its own scaling rules. A crucial difference between monofractals and multifractals is in their temporal evolution. In monofractals, large fluctuations of parameters (say, energy release events) are rare and do not determine mean values. In other words, time profiles are non-intermittent and evolution proceeds without catastrophes. On the contrary, in multifractals, the time profiles are highly intermittent, large fluctuations are not rare, and they determine mean values. The temporal energy release process is burst-like.

If so, the monofractal property of the CH magnetic field at scales above 2 Mm seems to be the most plausible reason why the averaged magnetic flux density, derived from observations with low resolution, does not correlate with the solar wind speed: the bulk of energy release dynamics, needed for the solar wind acceleration, occurs at smaller scales, where the magnetic field structure is entirely different.

Berger and colleagues (Berger *et al.*, 2004) observed a plage area with 0.1 arcsec resolution, and they report that the magnetic flux is structured into amorphous ribbon-like clusters with embedded knots of enhanced density, which seems to correspond to the notion of multifractality at small scales.

It is worth to mention that the property of monofractality of solar magnetic fields was known for a long time (see references in the previous section). Difficulties of describing magnetic structures with a single fractal dimension at the entire range of scales was also noticed (see, *e.g.*, Tarbell *et al.*, 1990; Janssen *et al.*, 2003), which actually is a signature of multifractality. Fractal analysis of high resolution magnetograms from VTT with 0.4 arcsec spatial resolution for a quiet sun area (Janssen *et al.*, 2003) revealed a break of self-similarity at scales of 1.3 Mm, which is very close to the scale found in this study.

For an active region and a plage area, our approach for deriving the filling factor of the magnetic field produced that $f(r) = 0.14 - 0.17$ at $r = 0.3$ Mm that generally agree with earlier reports. According to Tarbell *et al.* (1979), Schrijver (1987), Berger *et al.* (1995) and references herein, the magnetic filling factor is typically inside a range of 10 - 25%. In active regions, where the range of solar flares spreads over all observable scales, multifractality is also present at the same range of scales. This presents further evidence that energy release dynamics and the multifractality are mutually related properties of solar magnetic fields.

With the Hinode instrument in operation, many new phenomena related to the CH dynamics, coronal heating and solar wind acceleration will be discovered now, when the spatial scales less than 1000 km are available for analysis. Recent study of the evolution of network magnetic elements (Lamb *et al.*, 2008) proved that processes at sub-resolution scales are of vital importance for understanding the observed dynamics of magnetic flux.

Acknowledgements. Authors thank Spiro Antiochos, Len Fisk, Dennis Haggerty, Marco Velli, Yi-Ming Wang, Thomas Zurbuchen and the entire LWS/TR&T Heliospheric Focus Team for helpful discussions and initiation of this research. We also thank Rob Markel for valuable assistance in during the inversion process, and anonymous referees whose criticism and comments led to a significant improvement of the manuscript. We thank the ACE MAG and SWEPAM instrument teams and the ACE Science Center for providing the ACE data. SOHO is a project of international cooperation between ESA and NASA. Hinode is a Japanese mission developed and launched by ISAS/JAXA, collaborating with NAOJ as a domestic partner, NASA and STFC (UK) as international partners. Scientific operation of the Hinode mission is

conducted by the Hinode science team organized at ISAS/JAXA. This team mainly consists of scientists from institutes in the partner countries. Support for the post-launch operation is provided by JAXA and NAOJ (Japan), STFC (U.K.), NASA (U.S.A.), ESA, and NSC (Norway). Hinode SOT/SP inversions were conducted at NCAR under the framework of the Community Spectro-polarimetric Analysis Center (CSAC; <http://www.csac.hao.ucar.edu/>). This work was supported by NASA NNX07AT16G grant, and NSF grant ATM-0716512.

References

- Abramenko, V.I.: 2005, *Solar Phys.* **228**, 29.
- Abramenko, V.I.: 2008, In: Wang, P.(ed), *Solar Physics Research Trends*, Nova Science Publishers, Inc., New York, 95.
- Abramenko, V.I., Yurchyshyn, V.B., Wang, H., Spirock, T.J., Goode, P. R.: 2002, *Astrophys. J.* **577**, 487.
- Abramenko, V.I., Yurchyshyn, V.B., Wang, H., Spirock, T.J., Goode, P. R.: 2003, *Astrophys. J.* **597**, 1135.
- Abramenko, V. I., Fisk, L. A., Yurchyshyn, V. B.: 2006, *Astrophys. J.* **641**, L65.
- Abramenko, V.I., Yurchyshyn, V.B., Wang, H.: 2008, *Astrophys. J.* **681**, 1669.
- Arge, C.N., Luhmann, J.G., Odstrcil, D., Schrijver, C.J., Li, Y.: 2004, *J. Atmos. Solar Terr. Phys.* **66**, 1295.
- Baker, D., van Driel-Gesztelyi, L., Kamio, S., Culhane, J. L., Harra, L.K., Sun, J., Young, P.R., Matthews, S.A.: 2008, In: Matthews, S.A., Davis, J.M., Harra, L.K. (eds), *First Results From Hinode, ASP Conf. Ser.* **397**, 23.
- Balke, A.C., Schrijver, C.J., Zwaan, C., Tarbell, T.D.: 1993, *Solar Phys.* **143**, 215.
- Berger, T.E., Schrijver, C.J., Shine, R.A., Tarbell, T.D., Title, A.M., Scharmer, G.: 1995, *Astrophys. J.* **454**, 531.
- Berger, T. E., Rouppe van der Voort, L. H. M., Lofdahl, M. G., Carlsson, M., Fossum, A., Hansteen, V. H., Marthinussen, E., Title, A., Scharmer, G.: 2004, *Astron. Astrophys.* **428**, 613.
- Bumba, V., Klvana, M., Sykora, J.: 1995, *Astron. Astrophys.* **298**, 923.
- Delaboudiniere, J.-P., Artzner, G.E., Brunaud, J., Gabriel, A.H., Hochedez, J.F., Millier, F., et al.: 1995, *Solar Physics* **162**, 291.
- Fisk, L.A.: 1996, *J. Geophys. Res.* **101**, 15547.
- Fisk, L.A.: 2001, *J. Geophys. Res.* **106**, 15849.
- Fisk, L.A.: 2005, *Astrophys. J.* **626**, 563.
- Fisk, L.A., Zurbuchen, T. H., Schwadron, N.A.: 1999, *Astrophys. J.* **521**, 868.
- Frisch, U.: 1995, *Turbulence, The Legacy of A.N. Kolmogorov*, Cambridge University Press, Cambridge, 296.
- Hagenaar, H. J., DeRosa, M. L., Schrijver, C. J.: 2008, *Astrophys. J.* **678**, 541.
- Harvey, J., Krieger, A. S., Timothy, A. F., Vaiana, G. S.: 1975, *Oss. Mem. Oss. Arcetri* **104**, 50.
- Harvey, J. W., Sheeley, N. R., Jr.: 1979, *Space Sci. Rev.* **23**, 139.
- Harvey, K. L., Harvey, J. W., Sheeley, N. R., Jr.: 1982 *Solar Phys.* **79**, 149.
- Ichimoto, K., Lites, B., Elmore, D., Suematsu, Y., Tsuneta, S., Katsukawa, Y., et al.: 2008, *Solar Phys.* **249**, 233.

- Ireland, J., Gallagher, P.T., McAteer, R.T.J.: 2004, In: Dupree, A.K., Benz, A.O. (eds), *Stars as Suns: Activity, Evolution and Planets*, *IAU Symp.* **219**, 255.
- Janssen, K., Vogler, A., Kneer, F.: 2003, *Astron. Astrophys.* **409**, 1127.
- Lamb, D. A., DeForest, C. E., Hagenaar, H. J., Parnell, C. E., Welsch, B. T.: 2008, *Astrophys. J.* **674**, 520.
- Kamio, S., Hara, H., Watanabe, T., Matsuzaki, K., Shibata, K., Culhane, L., Warren, H.P.: 2007, *Publ. Astron. Soc. Japan* **59**, S757.
- Lawrence, J.K., Ruzmaikin, A.A., Cadavid, A.C.: 1993, *Astrophys. J.* **417**, 805.
- Longcope, D.W., Parnell, C.E.: 2008, *Solar Physics* **254**, 51.
- McAteer, R.T.J., Gallagher, P.T., Ireland, J.: 2005, *Astrophys. J.* **631**.
- Meunier, N.: 1999, *Astrophys. J.* **515**, 801.
- Moreno-Insertis, F., Galsgaard, K., Ugarte-Urra, I.: 2008, *Astrophys. J.* **673**, L211.
- Obridko, V. N., Shelting, B. D.: 1989, *Solar Phys.* **124**, 73.
- Obridko, V., Formichev, V., Kharshiladze, A. F., Zhitnik, I., Slemzin, V., Hathaway, D., Wu, S. T.: 2000, *Astron. Astrophys. Trans.* **18**, 819.
- Robbins, S., Henney, C. J., Harvey, J. W.: 2006, *Solar Phys.* **233**, 265.
- Scherrer, P.H., Bogart, R.S., Bush, R.I., Hoeksema, J.T., Kosovichev, A.G., Schou, J., *et al.*: 1995, *Solar Phys.* **162**, 129.
- Schrijver, C.J.: 1987, *Astron. Astrophys.* **180**, 241.
- Schrijver, C.J.: 2001, *Astrophys. J.* **547**, 475.
- Schrijver, C.J., Zwaan, C., Balke, A.C., Tarbell, T.D., Lawrence, J.K.: 1992, *Astron. Astrophys.* **253**, L1.
- Schrijver, C.J., Title, A.M.: 2001, *Astrophys. J.* **551**, 1099.
- Schrijver, C.J., DeRosa, M.L., Title, A.M.: 2002, *Astrophys. J.* **577**, 1006.
- Schrijver, C.J., DeRosa, M.L.: 2003, *Solar Phys.* **212**, 165.
- Schroeder, M.: 1991, *Fractals, Chaos, Power Laws*, W.H. Freeman and Company, New York, 429.
- Schwadron, N.A., McComas, D.J.: 2008, AGU, Fall Meeting, SH13B-1559.
- Sheeley, N.R., Jr., Harvey, J.W., Feldman, W.C.: 1976, *Solar Phys.* **49**, 271.
- Shimojo, M.: 2008, AGU, Fall Meeting, SH22A-0836.
- Suematsu, Y.: 2008, AGU, Fall Meeting, SH41B-1623.
- Tarbell, T.D., Title, A.M., Schoolman, S.A.: 1979, *Astrophys. J.* **229**, 387.
- Tarbell, T., Ferguson, S., Frank, Z., Shine, R., Title, A., Topka, K., Scharmer, G.: 1990, In: Stenflo, J.O. (ed.), *Solar Photosphere: Structure, Convection, and Magnetic fields*, *IAU Symp.* **138**, 147.
- Tsuneta, S., Ichimoto, K., Katsukawa, Y., Nagata, S., Otsubo, M., Shimizu, T., *et al.*: 2008, *Solar Phys.* **249**, 167.
- Vršnak, B., Temmer, M., Veronig, A.M.: 2007, *Solar Phys.* **240**, 315.
- Wang, Y.M., Sheeley, N.R.: 1990, *Astrophys. J.* **355**, 726.
- Wang, Y.M., Sheeley, N.R.: 1991, *Astrophys. J.* **375**, 761.
- Wang, Y.M., Lean, J., Sheeley, N.R.: 2000, *Geophys. Res. Lett.* **27**, 505.
- Wiegelmann, T., Solanki, S.K.: 2004, *Solar Phys.* **225**, 227.
- Wiegelmann, T., Xia, L. D., Marsch, E.: 2005, *Astron. Astrophys.* **432**, L1.

Table I. List of studied coronal holes and the corresponding parameters.

CH name	Culmination time	t_0 , doy	t_A , doy	Φ_{net} , 10^{21} Mx	B_{net} G	A , pixels	θ , deg	$\langle V_x \rangle$, km s^{-1}
CH191	2001Mar02/23:00	61.96	64.96	3.00	5.01	29145	17.2	559 \pm 16
CH230	2002Feb03/22:00	34.92	37.75	1.09	3.43	15408	-2.8	614 \pm 27
CH201	2002Mar02/17:00	61.71	64.38	3.03	4.27	34472	2.2	649 \pm 28
CH202	2002Mar29/18:00	88.75	91.08	2.61	4.22	30127	1.7	701 \pm 38
CH210	2002Apr28/23:00	118.96	122.63	0.84	3.85	10621	-19.6	462 \pm 14
CH231	2002Jul03/12:00	184.5	187.67	-0.92	-4.60	9721	-13.2	536 \pm 16
CH204	2002Nov01/17:00	305.71	309.04	1.49	2.54	28578	-6.3	549 \pm 16
CH350	2003Jan27/06:00	27.25	30.67	-0.24	-4.75	2555	1.6	507 \pm 14
CH302	2003Feb23/19:00	54.79	58.13	-2.04	-4.26	23176	7.1	560 \pm 18
CH303	2003Mar01/03:00	60.13	63.29	-1.65	-4.76	16856	14.2	530 \pm 32
CH304	2003Apr08/09:00	98.38	100.79	3.12	2.73	55633	-7.9	702 \pm 27
CH305	2003Apr24/07:00	114.29	117.71	-0.29	-2.67	5407	0.2	510 \pm 23
CH307	2003May03/19:00	123.79	126.38	3.07	3.23	46245	-11.1	693 \pm 23
CH354	2003May21/01:00	141.04	144.54	-1.43	-3.12	22381	-1.0	530 \pm 31
CH309	2003May25/19:00	145.79	148.21	-0.93	-5.59	8151	-20	701 \pm 31
CH312	2003Jun11/11:00	162.46	165.63	-0.47	-2.51	9260	-0.6	548 \pm 21
CH355	2003Aug10/01:00	222.04	224.63	-2.61	-2.43	52146	3.6	650 \pm 25
CH314	2003Aug20/19:00	232.79	235.04	4.57	2.66	83592	-4.9	741 \pm 28
CH356	2003Aug30/03:00	242.13	245.29	-0.40	-3.75	5191	7.8	526 \pm 20
CH357	2003Sep07/23:00	250.96	253.63	-3.17	-4.60	33515	-19.2	638 \pm 28
CH315	2003Sep16/08:00	259.33	261.5	4.84	2.98	79079	-4.2	749 \pm 35
CH317	2003Dec01/05:00	335.21	339.21	0.12	1.90	3207	-6.0	449 \pm 22
CH320	2003Dec18/19:00	352.79	355.79	-4.49	-3.98	54777	6.3	610 \pm 19
CH455	2004May17/10:00	138.42	141.75	0.21	2.07	5074	-2.7	519 \pm 24
CH456	2004May28/23:00	149.96	153.13	-0.58	-1.17	24452	13.0	549 \pm 17
CH457	2004May31/03:00	152.13	155.54	-3.03	-4.24	34826	-3.3	503 \pm 15
CH458	2004Jun05/01:00	157.04	160.96	-0.40	-3.73	5281	14.2	452 \pm 13
CH459	2004Jun12/10:00	164.42	167.75	0.31	1.83	8469	-9.8	542 \pm 25
CH460	2004Jul07/23:00	189.96	193.71	0.36	2.36	7540	11.4	491 \pm 20
CH461	2004Jul13/13:00	195.54	199.13	0.15	1.32	5590	2.8	518 \pm 22
CH462	2004Nov21/19:00	326.79	330.21	0.28	3.53	3967	16.0	513 \pm 17
CH412	2004Nov27/17:00	332.71	335.63	-2.47	-4.29	27994	-1.2	638 \pm 19
CH502	2005Feb15/07:00	46.29	49.54	-0.80	-3.24	12051	14.8	547 \pm 21
CH503	2005Apr17/02:00	107.08	110.42	0.45	2.90	7650	-9.5	523 \pm 22
CH554	2005May29/05:00	149.21	153.63	0.50	2.28	10710	-14.0	434 \pm 16
CH558	2005Jul26/10:00	207.42	210.58	-0.78	-2.08	18438	-5.4	559 \pm 31
CH563	2005Oct11/19:00	284.79	289.63	0.13	1.30	5075	1.9	372 \pm 19
CH564	2005Oct23/15:00	296.63	299.88	0.24	1.83	6557	-1.9	508 \pm 26
CH567	2005Dec26/15:00	360.63	363.04	-0.70	-1.75	19465	2.3	668 \pm 32
CH601	2006Jan12/19:00	12.79	16.71	0.41	1.95	10396	4.3	433 \pm 12
CH603	2006Feb12/03:00	43.13	46.79	0.29	2.48	5799	-8.3	535 \pm 21
CH604	2006Feb24/19:00	55.79	60.21	0.40	4.14	4813	-4.9	411 \pm 14
CH606	2006May03/09:00	123.38	126.88	0.78	1.33	28904	-4.0	600 \pm 27
CH607	2006Jul02/19:00	183.83	186.67	-0.91	-1.30	34120	2.0	593 \pm 24

Table II. SOHO/MDI magnetic measurements for a box inside CH204 coronal hole.

Type of magnetogram	B_{net} G	B_{tot} G	B_{n} G	Flux imbalance, %	$B_{\text{net}}(< p)$ G	Area above noise level, %
Full disk 1 min	4.53	19.5	17.3	23	1.11	4.1
Full disk 1 min smoothed	4.50	10.3	4.17	44	0.38	19
Full disk 5 min ave	4.48	12.1	9.3	37	0.84	6.1
Full disk 5 min ave smoothed	4.48	8.1	3.2	55	0.23	16
Hi res	3.88	12.4	8.9	31	1.64	6.6